

Direct observation of forbidden x-ray transitions from autoionizing levels in dense laser-produced plasmas

F. B. Rosmej,^{1,*} D. H. H. Hoffmann,^{2,3} W. Süß,² M. Geißel,² A. Ya. Faenov,⁴ and T. A. Pikuz⁴

¹Atomic Physics Laboratory, RIKEN, Wako, Saitama 351-0106, Japan

²GSI-Darmstadt, Institute of Plasma Physics, Planckstraße 1, D-64220 Darmstadt, Germany

³Technische Universität Darmstadt, Institute of Nuclear Physics, Schloßgartenstraße 9, D-64289 Darmstadt, Germany

⁴Multicharged Ions Spectra Data Center of VNIIFRI, Mendeleevo, 141570 Moscow Region, Russia

(Received 5 July 2000; revised manuscript received 25 September 2000; published 14 February 2001)

By means of high spectral and spatial resolution x-ray spectroscopic methods we have observed for the first time simultaneously two-electron and higher-order intercombination transitions from autoionizing levels in large scale optically thick laser produced plasmas. Intercombination transitions as well as the two-electron op-satellite transitions in Li-like ions have anomalous large intensities (up to a factor of 14). Sophisticated non-Maxwellian opacity simulations treating extended configuration interaction atomic data employing the MARIA-code reveal, however, good agreement among forbidden transitions.

DOI: 10.1103/PhysRevA.63.032716

PACS number(s): 32.80.Dz, 32.70.Fw, 32.30.Rj

I. INTRODUCTION

It has early been realized [1] that transitions from autoionizing levels (so-called dielectronic satellites) of highly charged ions provide an outstanding plasma temperature diagnostic; under the conditions of an optically thin, low-density Maxwellian plasma the intensity ratio between a resonance line and its adjacent dielectronic satellites is a function of the electron temperature only. However, many of these assumptions are often not fulfilled, e.g., in pinch plasmas, laser produced plasmas, hohlraum plasmas, and ion-beam driven matter. Therefore numerous basic methods of dielectronic satellite diagnostics have been developed and successfully applied to dense [2–5] and non-Maxwellian plasmas [6–12].

Recently Elton and co-workers [13] observed in laser produced plasmas at the TRIDENT facility in Los Alamos anomalous high (order of magnitude) intensity of the two-electron transitions from Li-like and He-like autoionizing levels: $1s2s^2 \rightarrow 1s^2 2p + h\nu$ (so-called “op” satellites) and $2s^2 \rightarrow 1s2p + h\nu$. However, despite complex spectra analysis, the origin of these phenomena remained unexplained, thereby questioning the entire approach of widely spread standard plasma diagnostics based on *K*-shell x-ray emission lines.

The present paper is devoted to the urgent need for the clarification of these discrepancies. Particular open questions are, first, whether these discrepancies are typical for two-electron transitions only and, second, the basic interpretation of their anomalous intensity itself; are two-electron transitions too large compared to standard modelings or do there exist mechanisms that suppress all lines with the exception of the two-electron transitions? We have succeeded with the basic understanding of these questions; the resolution of these problems are found exploring highly resolved forbid-

den satellite transitions for opacity free diagnostics.

II. EXPERIMENTAL SETUP

Experiments have been performed at the nhelix-laser test bed facility at GSI. A 50 J, 15-ns long pulse from the Nd-glass YAG laser at $\lambda = 1.064 \mu\text{m}$ with a spot size of about $500 \mu\text{m}$ was focused onto a massive Al target for the production of large scale (mm size) dense ($n_e \approx 10^{21} \text{cm}^{-3}$) laser produced plasmas. A particular feature of such plasmas is the large line center optical thickness τ_0 for a line transition $j \rightarrow i$:

$$\tau_{0,ij} = \frac{1}{4} \lambda_{ji}^2 \frac{g_j}{g_i} A_{ji} n_i \left\{ 1 - \frac{g_i n_j}{g_j n_i} \right\} \varphi_{ij}(\omega = \omega_{ji}) L_{\text{eff}}, \quad (1)$$

where λ is the wavelength, A the radiative decay, g_j and g_i are the statistical weights of the upper and lower levels, respectively, φ is the line profile including natural, Doppler, and collisional broadening, and L_{eff} is the effective photon path length. For example, the He-like resonance line $W = 1s2p \ ^1P_1 \rightarrow 1s^2 \ ^1S_0 + h\nu$ typically has a line center optical thickness τ_0 of several hundreds and even the intercombination line $Y = 1s2p \ ^3P_1 \rightarrow 1s^2 \ ^1S_0 + h\nu$ is optically thick, $\tau_0 > 1$. Because the line center optical thickness is proportional to the radiative decay rate we have a tool to depress the intensity of allowed transitions (with high values of optical thickness) while keeping the intensity of forbidden ones essentially opacity free. The experimental realization, however, is very complicated because: (a) forbidden transitions originating from autoionizing levels are strongly blended with many other lines and (b) the plasma inhomogeneity drastically changes the spectral distribution and the optical thickness.

We have succeeded with these obstacles applying high-resolution x-ray imaging methods. Space resolved x-ray spectra have been recorded by means of spherically bent mica crystals [14] with curvature radius of $R_c = 150 \text{mm}$ and Kodak DEF-5 x-ray film (grain size $1.6 \mu\text{m}$). In order to protect the film from the visible light, 2 polypropylene foils (each of thickness $1 \mu\text{m}$) covered from each side with Al (each sheath of thickness of $0.2 \mu\text{m}$) were used. The distance

*Permanent address: Technische Universität Darmstadt. Email address: rosmej@yahoo.de

target crystal and crystal film were $a=340$ mm and $b=129$ mm, respectively. The central Bragg angle was $\theta=53.4^\circ$ (second order of reflection) and the angle between the central ray and the target surface was 45° . A 10.000 dpi (dots per inch) drum scanner (EUROCORE) was used to obtain the space and spectrally resolved photon exposure from the x-ray images. The effective spectral resolution was about $\lambda/\delta\lambda\approx 3000$. The spatial resolution was adjusted in order to meet two criteria: first, to receive a large field of view and, second, to resolve the characteristic spatial variations; 1 px (pixel) corresponded to a real distance onto the target of about $32\ \mu\text{m}$ [$2.54\ \mu\text{m}\times(10.000/3000)\times(a/b)/\sin 45^\circ$] was chosen. Spectra have been corrected for crystal reflectivity, filter transmission, and film response using the program SCALE. SCALE also accounts for possible nonlinearity in the experimental wavelengths scale performing polynomial dispersion scale fitting with three reference lines at $\lambda=0.784\ 81$ nm, $0.807\ 89$ nm, and $0.834\ 04$ nm.

Figure 1(a) shows the x-ray image of Al and Figs. 1(b) and 1(c) show the spectrum from the central trace (corresponding to the target surface). The spectrum contains the He-like W and Y lines as well as numerous dielectronic satellite transitions to be discussed below.

III. ATOMIC DATA OF FORBIDDEN X-RAY TRANSITIONS FROM AUTOIONIZING LEVELS

The high-resolution spectroscopy enabled us to separate four different classes of satellite transitions:

(1) Allowed transitions: a resonance transition $n=2\rightarrow 1$ screened by a spectator electron in the $n'=2$ shell, e.g., $1s2p^2\ ^2D\rightarrow 1s^22p\ ^2P+h\nu$ [Fig. 1(b)];

(2) two-electron transitions: transitions changing main (n) and orbital (l) quantum numbers of simultaneously two electrons (arising from configuration interaction), e.g., $1s2s^2\ ^1S\rightarrow 1s^22p\ ^2P+h\nu$ [2d, e in Fig. 1(c)];

(3) intercombination transitions: dipole transitions $n=2\rightarrow 1$ changing the spin ($\Delta S=1$) arising from the breakdown of the LS coupling scheme, e.g., $1s(2s2p\ ^3P)^4P\rightarrow 1s^22s\ ^2S+h\nu$ [2b, c in Fig. 1(c)];

(4) higher-order intercombination transitions: dipole transitions $n=2\rightarrow 1$ changing the spin ($\Delta S=1$) of the optical electron (transition electron) with configurations having spectator electrons in shells with $n'>2$ (also arising from the breakdown of the LS coupling scheme), e.g., $(1s2p\ ^3P)3d\ ^2D\rightarrow 1s^23d\ ^2D+h\nu$ [3a in Fig. 1(c)] and $(1s2p\ ^3P)3p\ ^2P\rightarrow 1s^23p\ ^2P+h\nu$ [3b in Fig. 1(c)].

These simultaneous observations in dense laser produced plasmas have not been reported in the literature. Consequently only little attention has been paid to accurate atomic data. Well-established methods for atomic data calculations like the multiconfiguration Z expansion including relativistic and QED effects (MZ) [15], the multiconfiguration Hartree-Fock method including relativistic corrections to the wave function and Breit energy corrections (HFR) [16], and the multiconfiguration Dirac-Fock method (MCDF) [17] are employed in the present work.

Table I shows the results of the present calculations for Al for the $1s2l2l'$ configurations and Table II those for the

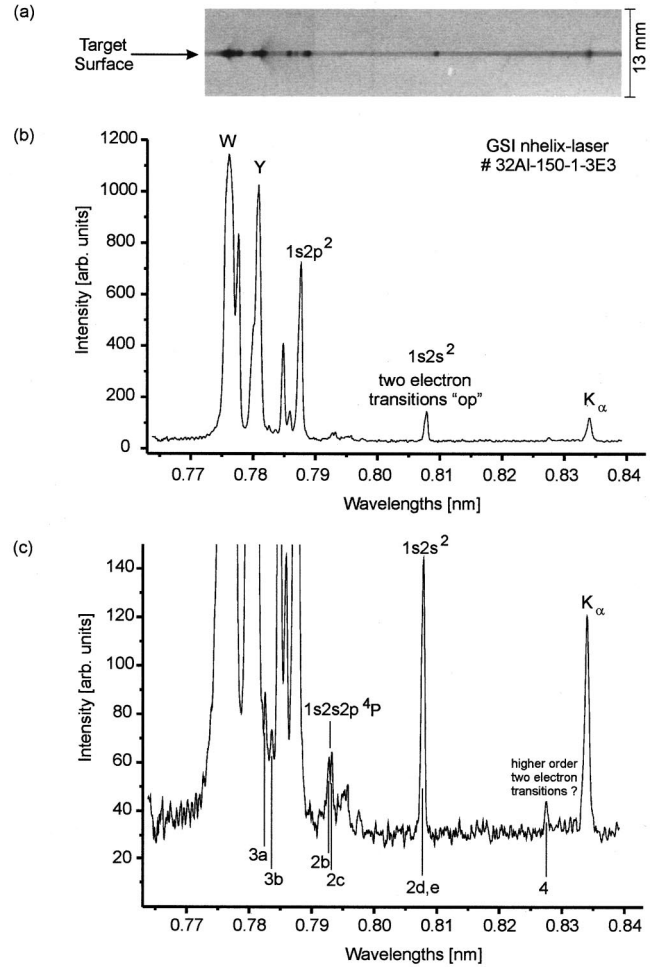


FIG. 1. (a) Space resolved high-resolution x-ray spectrum of Al. The horizontal line corresponds to x-ray emissions from plasmas near the target surface. Al II K_α -lines originate from hot electrons returning from the expanding plasma and penetrating into the massive Al target. (b) Spectrum from the target surface. The two-electron transitions $1s2s^2\ ^2S_{1/2}\rightarrow 1s^22p\ ^2P_{1/2,3/2}+h\nu$ have anomalous high intensities compared to the dipole transitions $1s2p^2\rightarrow 1s^22p+h\nu$. (c) Enhanced scale of Fig. 1(a). Anomalous high intensity is seen also from intercombination and two-electron transitions (2a–2e, 3a–3b, 4) originating from Li-like autoionizing levels.

$1s2l3l'$ configurations. It can be seen, that transition probabilities A agree on a 20%–30% level. By means of spectra fitting methods to be described below, we found that almost all wavelengths of the MZ method coincided very well with the experiment without any additional line shifts. For example, the experimental wavelengths $\lambda(3a)=7.8250(10)$ and $\lambda(3b)=7.8357(10)$ coincide very well with the calculations. HFR, MCDF as well as Refs. [18,19] show up with systematically higher wavelengths by 3–8 mÅ (compared to MZ values) and agreed with each other by about 1–3 mÅ. The autoionizing probability Γ gives rise to the so-called dielectronic capture, namely,

$$1s^2+e\rightarrow 1s2lnl'.$$

TABLE I. Observed [see Figs. 1(b) and 1(c)] quartet intercombination transitions (2a–2c) and two-electron transitions (2d, 2e) originating from Li-like Al autoionizing levels $1s2l2l'$. Atomic data are present calculations by means of the MZ method (first values), the HFR method (second values), and the MCDF method (third values). The ${}^4P_{5/2}$ state radiatively decays only via a magnetic quadrupole transition whereas the Auger transition is due to Breit interaction [18,19].

Key	Transition	$\lambda/10^{-10}$ m	A/s
2a	$1s(2s2p\ {}^3P)^4P_{5/2}-1s^2 2s\ {}^2S_{1/2}$	7.9299/7.9333/7.9412	-/-/1.91 $\times 10^7$
2b	$1s(2s2p\ {}^3P)^4P_{3/2}-1s^2 2s\ {}^2S_{1/2}$	7.9323/7.9359/7.9437	$1.57\times 10^{10}/1.18\times 10^{10}/1.57\times 10^{10}$
2c	$1s(2s2p\ {}^3P)^4P_{1/2}-1s^2 2s\ {}^2S_{1/2}$	7.9333/7.9374/7.9446	$5.95\times 10^9/4.48\times 10^9/6.06\times 10^9$
2d	$1s(2s^2\ {}^1S)^2S_{1/2}-1s^2 2p\ {}^2P_{1/2}$	8.0764/8.0784/8.0873	$4.17\times 10^{11}/5.53\times 10^{11}/4.66\times 10^{11}$
2e	$1s(2s^2\ {}^1S)^2S_{1/2}-1s^2 2p\ {}^2P_{3/2}$	8.0802/8.0821/8.0910	$7.68\times 10^{11}/1.02\times 10^{12}/8.57\times 10^{11}$

The associated dielectronic recombination rate $\langle DR \rangle$ for the transitions

$$1s^2 + e \rightarrow 1s2lnl' \rightarrow \begin{cases} 1s^2 2l + h\nu \\ 1s^2 nl' + h\nu \end{cases}$$

is given by

$$\langle DR \rangle = \alpha Q \frac{\exp(-E_s/kT_e)}{(kT_e)^{3/2}}. \quad (2)$$

E_s is the capture energy in [eV], kT_e the electron temperature in [eV], and $\alpha = 1.656 \times 10^{-22} \text{ cm}^3 \text{ s}^{-1}$. Q is the so-called satellite intensity factor:

$$Q_{ji} = \frac{g_j A_{ji} \Gamma_j}{\sum A + \sum \Gamma} \quad (3)$$

(g_j and Γ_j are the statistical weight and autoionizing rate of the autoionizing level, A_{ji} is the transition probability, and the sums in the denominator are over all decaying processes of the upper level j). Comparison of the autoionizing rates Γ calculated with the various methods discovered an agreement within only a factor of 2 between the GRASP/HFR and MZ method. We therefore have also cross checked our calculations with those of Refs. [20,21]. Their tables do not contain calculations for Al but for Si. We therefore have performed our calculations also for Si. The finding is that the HFR autoionizing rates agree with those of Refs. [20,21] on a 20%–30% level [with exception of the $1s(2s2p\ {}^3P)^4P_{3/2}$

level where the autoionizing of Ref. [20] is smaller by four orders of magnitude while MZ, HFR, and Ref. [21] agree within a factor of 2, note, however, that the absolute value of Γ is very low].

This established level of atomic data agreement allows the investigation of the anomalous high (order of magnitude) intensities of forbidden lines. Unfortunately the population densities of the upper levels of forbidden satellites is not dominated by the (a) dielectronic capture $1s^2 + e \rightarrow 1s2lnl'$ only but rather by (b) inner-shell excitations $1s^2 2l, 3l' + e \rightarrow 1s2l3l' + e$, (c) collisional transfer between the autoionizing levels $1s2l3l'LSJ + e \rightarrow 1s2k3k'L'S'J' + e$, and (d) and three-body recombination $1s2l + e + e \rightarrow 1s2lnl' + e$ from the singly excited levels of the parent resonance line [4]. For further analysis we therefore employ multilevel metastable resolved, multi-ion stage collisional radiative spectra simulations described below to treat properly these various channels.

IV. NON-MAXWELLIAN SPECTRA SIMULATIONS

The observed K_α transition (Fig. 1) from AlII at $\lambda = 0.833\ 97/0.834\ 20$ nm directly indicates the presence of hot electrons returning from expanding plasma to the target surface due to a self-generated magnetic field. The massive target is illuminated like an x-ray tube. Near the central line [see Fig. 1(a) ‘‘Target surface’’] strong K_α emission extends up to about 600 μm but is still observable up to about 1200 μm .

TABLE II. Observed [see Figs. 1(b) and 1(c)] higher-order doublet intercombination transitions (3a, 3b) originating from Li-like Al autoionizing levels $1s2l3l'$. Atomic data are present calculations by means of the MZ method (first values), the HFR method (second values), and the MCDF method (third values).

Key	Transition	$\lambda/10^{-10}$ m	A/s
3a	$(1s2p\ {}^3P)3d\ {}^2D_{5/2}-1s^2 3d\ {}^2D_{3/2}$	7.8245/7.8304/7.8332	$2.43\times 10^{11}/1.48\times 10^{11}/1.31\times 10^{11}$
	$(1s2p\ {}^3P)3d\ {}^2D_{3/2}-1s^2 3d\ {}^2D_{3/2}$	7.8247/7.8308/7.8335	$2.25\times 10^{11}/3.14\times 10^{11}/3.01\times 10^{11}$
	$(1s2p\ {}^3P)3d\ {}^2D_{5/2}-1s^2 3d\ {}^2D_{5/2}$	7.8248/7.8307/7.8335	$1.80\times 10^{11}/3.06\times 10^{11}/2.96\times 10^{11}$
3b	$(1s2p\ {}^3P)3p\ {}^2P_{1/2}-1s^2 3p\ {}^2P_{1/2}$	7.8349/7.8403/7.8437	$1.12\times 10^{12}/1.09\times 10^{12}/8.96\times 10^{11}$
	$(1s2p\ {}^3P)3p\ {}^2P_{3/2}-1s^2 3p\ {}^2P_{1/2}$	7.8349/7.8402/7.8436	$4.92\times 10^{11}/4.32\times 10^{11}/3.42\times 10^{11}$
	$(1s2p\ {}^3P)3p\ {}^2P_{1/2}-1s^2 3p\ {}^2P_{3/2}$	7.8359/7.8414/7.8447	$3.65\times 10^{11}/3.94\times 10^{11}/2.87\times 10^{11}$
	$(1s2p\ {}^3P)3p\ {}^2P_{3/2}-1s^2 3p\ {}^2P_{3/2}$	7.8360/7.8412/7.8446	$1.33\times 10^{12}/1.37\times 10^{12}/1.12\times 10^{12}$

We therefore consider collisional radiative spectra simulations for non-Maxwellian plasmas employing the MARIA code [12]. The upper-level densities n_j are determined from a system of differential rate equations

$$\frac{dn_j}{dt} = \sum_{i=1}^N n_i \{W_{ij} + A_{ij}\Lambda_{ij} + P_{ij}^{iz} + R_{ij}^{\text{stim}}\} - n_j \sum_{k=1}^N \{W_{jk} + A_{jk}\Lambda_{jk} + P_{ik}^{iz} + R_{ik}^{\text{stim}}\}. \quad (4)$$

We note, that near the target surface, transient effects are not expected to be of importance due to the long laser pulse duration. Taking an characteristic electron density of $n_e = 3 \times 10^{20} \text{ cm}^{-3}$ and the time duration of $\tau = 10^{-8} \text{ s}$ we estimate the confinement parameter to be

$$n_e \tau \approx 3 \times 10^{12} \text{ cm}^{-3} \text{ s}.$$

This value is one order of magnitude larger above which quasistationary conditions are established. The matrix W is given by

$$W_{ij} = C_{ij} + Cp_{ij} + R_{ij} + I_{ij} + Ip_{ij} + T_{ij} + \Gamma_{ij} + DC_{ij}, \quad (5)$$

where C is the collisional excitation/deexcitation matrix, I the collisional ionization matrix, T the three-body recombination, R the radiative recombination, Γ the autoionization, DC the dielectronic capture, A the spontaneous radiative decay matrix, and ion-ion (atom) collisions (excitation/deexcitation and ionization) are described by the matrixes Cp and Ip . The indices “ ij ” indicate the transition from level i to level j , if a matrix element physically does not exist, its value is zero. The radiation terms for line transitions are contained in $\Lambda(L_{\text{eff}})$ where L_{eff} is the effective photon path length [22]. Line overlapping and asymmetric repumping is calculated by taking the sum over the single absorption coefficients κ_{ij} :

$$\kappa(\omega) = \sum_{ij} \kappa_{ij}(\omega). \quad (6)$$

P^{iz} and R^{stim} are the rate matrices for the photoionization and stimulated radiative recombination. For optically thick plasmas, the set of differential equations becomes nonlinear, because $\Lambda_{ij} = \Lambda_{ij}(n_i, n_j)$. The spectral distribution $I(\omega)$ is calculated according to

$$I(\omega) = \sum_{i,j} I_{ij}(\omega) = \sum_{i,j} n_i A_{ij} \Lambda_{ij} \Phi_{ij}^{\text{norm}}(\omega). \quad (7)$$

Φ_{ij}^{norm} is the normalized optically thick line profile [4,12], which provides self-consistency of the level populations along with the spectral distribution.

In non-Maxwellian plasmas, hot electrons have essential influence on inner-shell excitation and the ionic populations of different charge states. The respective non-Maxwellian rate coefficients of collisional excitation, deexcitation, ion-

ization, three body recombination, dielectronic capture and radiative recombination rate coefficients C entering the W matrix are given by

$$C_{ij} = \int_{\Delta E}^{\infty} dE \sigma_{ij}(E) V(E) F(E), \quad (8)$$

where σ_{ij} is the electron collisional excitation cross section, ΔE is the threshold energy, $F(E)$ is the electron distribution function, and $V(E)$ is the relative velocity of the electrons and the ions atoms. The corresponding deexcitation rate coefficient R is given by

$$C_{ji} = \frac{g_i}{g_j} \int_0^{\infty} dE \sigma_{ij}(E + \Delta E) \frac{E + \Delta E}{E} V(E) F(E), \quad (9)$$

where g_j and g_i are the statistical weights of the upper and lower level, respectively. The radiative recombination rate coefficient is given by

$$R_{i+1,i} = n_e \frac{g_i}{g_{i+1}} \frac{1}{\sqrt{2} m_e^{3/2} c^2} \int_0^{\infty} dE \times \sigma_{i,i+1}^i(E_i + E) \frac{(E_i + E)^2}{\sqrt{E}} F(E), \quad (10)$$

where $\sigma_{i,i+1}^i$ is the photoionization cross section, n_e and m_e are the electron density and mass, respectively, and c the velocity of light. The dielectronic capture is a resonance process and the respective non-Maxwellian rate coefficient D is therefore given by

$$D_{jk}^c = \frac{\pi^2 \hbar^3}{\sqrt{2} m_e^{3/2}} \frac{g_j}{g_k} \frac{\Gamma_{jk}}{\sqrt{E_s}} F(E_s), \quad (11)$$

where E_s is the capture energy, and Γ_{jk} the autoionizing rate from level j to level k . The collisional ionization rate coefficient I is given by

$$I_{ij} = \int_{E_i}^{\infty} dE \sigma_{ij}^I(E) V(E) F(E), \quad (12)$$

where $\sigma_{ij}^I(E)$ is the ionization cross section and E_i the ionization energy. The non-Maxwellian three body recombination rate T requires rather time consuming double integrals due to the necessity of two electron distribution functions:

$$T_{ij} = \frac{\pi^2 \hbar^3}{m_e^2} \frac{g_i}{g_j} \int_0^{\infty} dE_1 \int_0^{\infty} dE_2 \frac{E}{\sqrt{E_1 E_2}} \times \sigma_{ij}^I(E, E_1) F(E_1) F(E_2). \quad (13)$$

$\sigma_{ij}^I(E, E_1)$ is the double-differential ionization cross section. Equations (8)–(13) are exact. Terms like “beam fraction f ,” “hot-electron temperature T_{hot} ,” and “bulk electron temperature T_{bulk} ” originate from numerous experimental obser-

vations at various laser installations; the electron distribution function $F(E)$ can reasonably be approximated with two Maxwellians $F_M(E)$:

$$F(E) = (1-f)F_M(T_{\text{bulk}}, E) + fF_M(T_{\text{hot}}, E), \quad (14)$$

$$F_M(T, E) = \frac{2\sqrt{E} \exp(-E/kT)}{\sqrt{\pi} (kT)^{3/2}}. \quad (15)$$

The beam fraction f has to be defined by

$$f = \frac{g}{1+g}, \quad (16)$$

$$g = \frac{n_e(T_{\text{hot}})}{n_e(T_{\text{bulk}})} \quad (17)$$

in order to provide the normalization

$$\int_0^\infty F(E) dE = 1. \quad (18)$$

Although Eqs. (14)–(18) are also quite general, the interpretation of T_{bulk} and T_{beam} as bulk and beam “temperature” are only meaningful if $T_{\text{bulk}} \ll T_{\text{beam}}$ and $f \ll 1$.

The adopted ionic level system is rather extended in order to describe properly ionic populations of various charge states as well as transitions from singly and doubly excited states; included are all ground states of Al I–Al XIV, H-like levels nl with $n=1-4$ and $l=0-3$, He-like levels $1snl$ with $n=1-4$, $l=0-3$, Li-like levels $1s^2nl$ with $n=2-4$, $l=0-3$ as well as effective dielectronic and radiative recombination rates for all charge states. Also included are all dipole transitions with $\Delta S=0$ (resonance) and $\Delta S=1$ (intercombination) as well as two-electron transitions from the autoionizing states $2lnl'$ with $n=2-4$, $1s2lnl'$ with $n=2-4$.

Figure 2 demonstrates the influence of different fractions f [defined by Eqs. (14)–(18)] of hot electrons on the spectrum. Figure 2(a) is calculated for a Maxwellian electron distribution function ($f=0$). Strong overall satellite emission is seen that even exceeds the resonance line intensity. The phenomenon of dielectronic satellite accumulation near the position of usual resonance (lower spectrum of Fig. 3) lines have been explored recently [4,23] and is essentially connected with low-temperature and large resonance line opacity. Starting with a beam fraction of $f=10^{-6}$ [Fig. 2(b)], hot electrons influence the emission spectrum. With increasing beam fraction [Figs. 2(c) and 2(d)] resonance line W and intercombination line Y are the dominating spectral features.

V. PLASMA DIAGNOSTICS BASED ON FORBIDDEN X-RAY SATELLITE TRANSITIONS

Figure 3 shows the simulations for characteristic parameters of laser produced plasmas. The upper spectrum of Fig. 3 is calculated for an optically thin plasma; practically no forbidden satellite transitions are observable. Taking into account the optical thickness for a large scale plasma, forbid-

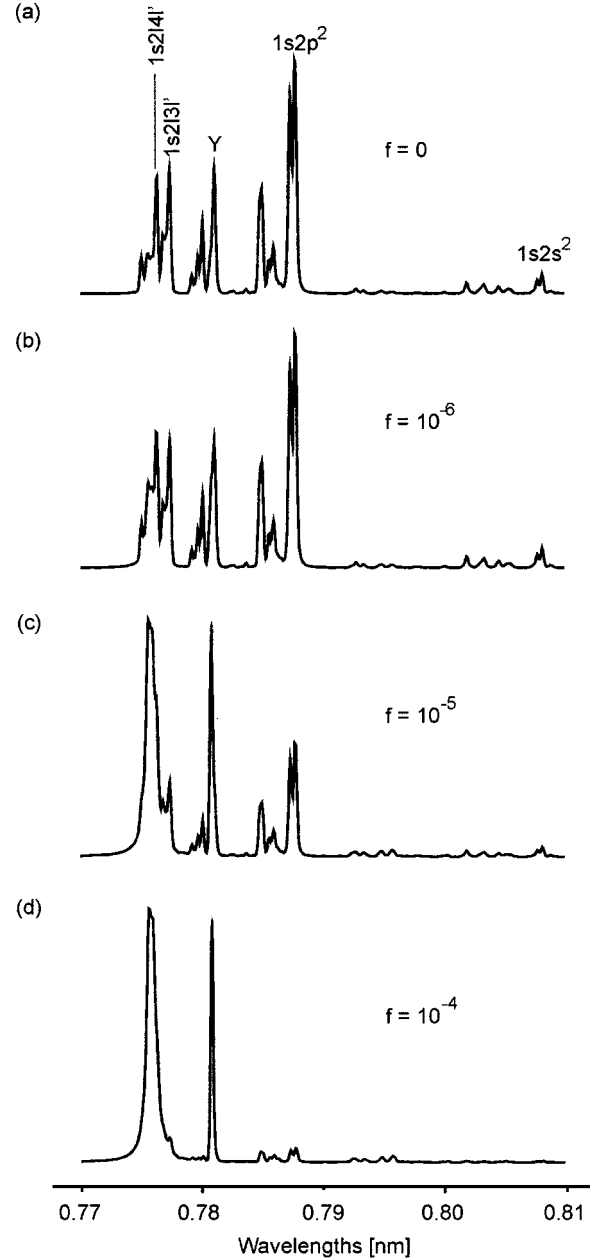


FIG. 2. Influence of hot electrons on the K -shell soft x-ray emission spectrum of Al in the spectral interval from 0.77–0.81 nm for different beam fractions f . Simulation parameters are $T_{\text{bulk}} = 100$ eV, $n_e = 2 \times 10^{20} \text{ cm}^{-3}$, $L_{\text{eff}} = 1000 \mu\text{m}$, $T_{\text{hot}} = 2$ keV, and $\lambda/\delta\lambda_{\text{app}} = 5000$.

den satellites become visible because transitions with high oscillator strengths are suppressed by opacity and transitions with low ones are marginally affected. However, the forbidden transitions have still too low intensity [about a factor of 3, compare Fig. 1(b) with the lower curve in Fig. 3] to match the experimental observation.

Table III provides insight to the line center optical thickness values τ_0 of various transitions from singly and doubly excited levels. The resonance line W has opacity values of several hundreds and even the intercombination line Y is optically thick ($\tau_0 \approx 1$). Even more interesting is the large

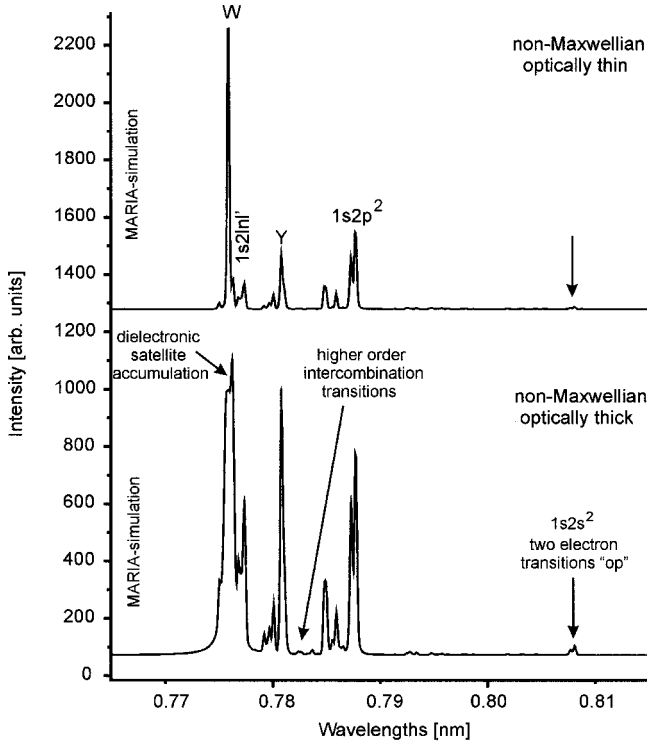


FIG. 3. Exploring the possible mechanism of anomalous high-intensity forbidden transitions. The upper spectrum shows a non-Maxwellian optically thin spectrum simulation (apparatus resolution $\lambda/\delta\lambda_{\text{app}}=5000$, electron density $n_e=2\times 10^{20}\text{ cm}^{-3}$, electron temperature $kT_{\text{bulk}}=140\text{ eV}$, photon path lengths $L_{\text{eff}}=0\text{ }\mu\text{m}$, hot-electron temperature $kT_{\text{hot}}=2\text{ keV}$, hot-electron fraction $f_{\text{hot}}=1.5\times 10^{-4}$) whereas the lower spectrum is calculated for a non-Maxwellian optically thick ($L_{\text{eff}}=1000\text{ }\mu\text{m}$) plasma. The contrast of these simulations shows that photoabsorption may lead to a relative rise of the forbidden transitions.

opacity of the $1s2l2l'$ satellites, τ_0 values up to 5 are encountered. Such values lead to rather effective photoabsorption due to the high autoionizing rates that act like a depopulating mechanism of the upper level. Consider, e.g., the transition $1s[2p^2\ ^1D] \ ^2D_{5/2} \rightarrow 1s^22p\ ^2P_{3/2} + h\nu$; $A=1.3\times 10^{13}\text{ s}^{-1}$, $\Gamma=1.5\times 10^{14}\text{ s}^{-1}$. The probability P of reemission after one act of photoabsorption is very low:

$$P = \frac{A}{A + \Gamma + C} \leq 0.08. \quad (19)$$

Dense large scale plasmas lead therefore to rather complicated photoabsorption phenomena. We note, that effects of dielectronic satellite absorption have directly been observed

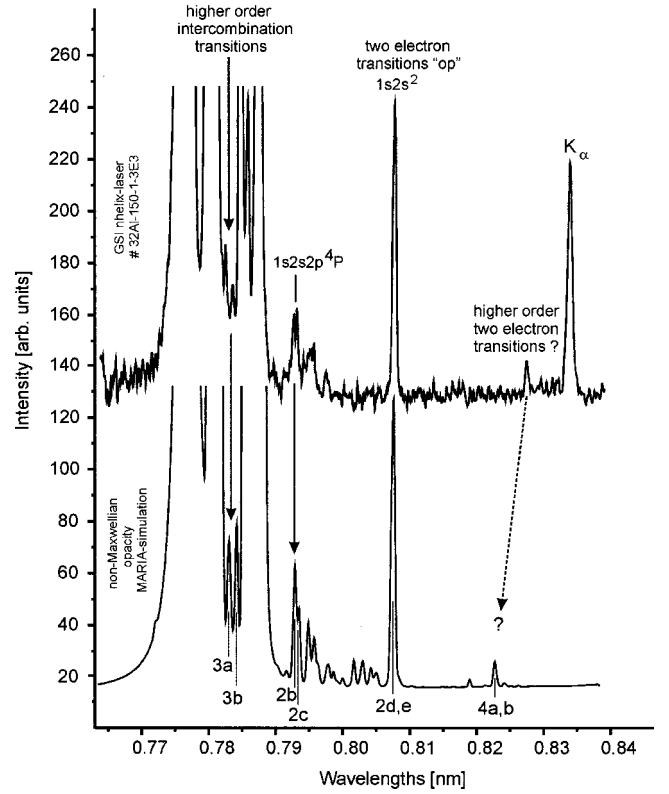


FIG. 4. The calculation of forbidden satellite transitions from various autoionizing levels results in a good agreement between the experimental spectrum (upper curve) and the non-Maxwellian opacity MARIA-code simulation (lower curve): $\lambda/\delta\lambda_{\text{app}}=2000$, $n_e=2\times 10^{20}\text{ cm}^{-3}$, $kT_e=140\text{ eV}$, $L_{\text{eff}}=1000\text{ }\mu\text{m}$, $kT_{\text{hot}}=2\text{ keV}$, and $f_{\text{hot}}=1.5\times 10^{-4}$. The coincidence demonstrates the advantageous diagnostic properties of forbidden radiative transitions from autoionizing levels in optically thick plasmas.

recently [24,4] and diagnostic methods were proposed and applied to laser produced plasma experiments [4].

Forbidden satellite transitions became also of large interest in experiments with slow heavy-ion-beams interacting with capillaries [18,19]. The enhanced emission from metastable levels shows an interesting similarity to our experiments; while in slow heavy-ion-beam experiments the metastables are selected by the time-of-flight method (allowed transitions have decayed after μm distances while forbidden transitions survive) whereas in large scale optically thick plasmas the allowed transitions are suppressed by opacity.

In order to describe the forbidden satellite emission rather than the allowed ones in a simulation we have taken into account all transitions arising from an extended configuration interaction calculation including simultaneously the levels

TABLE III. Line center opacities τ_0 of various transitions for an electron temperature of $kT_e=100\text{ eV}$, $n_e=2\times 10^{20}\text{ cm}^{-3}$, and $L_{\text{eff}}=1000\text{ }\mu\text{m}$ [e.g., $O(-3)$ means that τ_0 is of the order of 10^{-3}].

Transitions	W	Y	$1s2p^2$	$1s2l3l'$	$1s2l4l'$	He $_{\gamma}$ -sat.	He $_{\delta}$ -sat.
τ_0	3.7×10^2	1.1×10^0	1-5	$O(-2)$	$O(-2)$	$O(-3)$	$O(-3)$

$1s^2nl$ and $1s2lnl'$ with $n=2-7$ and $l=0-6$ (that means autoionizing levels up to $1s2p7i$ are included). In addition the K_α $n=2$ satellites for Be-, B-, and C-like Al ions are taken into account to provide a clear identification of the transitions 2b–e irrespective of possible line overlapping effects.

The space resolved results of Fig. 1(a) show, that forbidden line emissions do not “expand” like the W and Y lines and concentrate near the target surface only. Due to negligible opacity, space integration effects are entirely negligible. We therefore assume one set of parameters only. The results are shown in Fig. 4. The comparison between the experiment and the simulation demonstrates a surprisingly good agreement among the forbidden lines. In particular the higher-order intercombination transitions (3a,b), the quartet intercombination transitions (2b,c), and the two-electron transitions (2d,e) are well described with a unique set of parameters. All line intensities agree down to a 20% level (better agreement is not expected due to the inaccuracy of the atomic data described above).

The extended configuration interaction calculations gives rise to rather unexpected higher-order two-electron transitions of the type $1s2/3l' \rightarrow 1s^24l'' + h\nu$, e.g., indicated as “4a,b” in the lower spectrum of Fig. 4. The experimental spectrum also indicates a rather narrow transition between 0.82 and 0.83 nm. Although the intensities of the transitions

$4ab = (1s2p^3P)3d^2D \rightarrow 1s^24f^2F + h\nu$ coincide rather well, the line identification, however, is not clear because the wavelengths are expected to coincide within 10 mÅ. The calculated position of the lines 4a,b are, however, smaller by about 35 mÅ. Such types of transitions are rather sensitive to the type of configuration interaction included and are not well known at present.

VI. CONCLUSION

In conclusion we have observed for the first time simultaneously anomalous high intensity x-ray intercombination and two-electron transitions of even higher order from autoionizing levels in dense laser produced plasmas. We have demonstrated that configuration interaction atomic data equipped non-Maxwellian opacity simulations of forbidden satellite lines allow to reach an agreement on a 20% level, which was also shown to be the present level of agreement between various atomic structure codes. Opacity free diagnostics based on forbidden satellite transitions have been developed and successfully applied to experimental findings.

ACKNOWLEDGMENT

The authors thank Professor Y. Yamazaki for his interest in the present work and for fruitful discussions.

-
- [1] A. H. Gabriel, *Mon. Not. R. Astron. Soc.* **160**, 99 (1972).
 - [2] A. V. Vinogradov, I. Yu. Skobelev, and E. A. Yukov, *Kvant. Electron. (Moscow)* **2**, 1165 (1975) [*Sov. J. Quantum Electron.* **5**, 630 (1975)].
 - [3] V. J. Jacobs and M. Blaha, *Phys. Rev. A* **21**, 525 (1980).
 - [4] F. B. Rosmej *et al.*, *J. Quant. Spectrosc. Radiat. Transf.* **58**, 859 (1997).
 - [5] F. B. Rosmej and J. Abdallah, Jr., *Phys. Lett. A* **245**, 548 (1998).
 - [6] A. S. Shlyaptseva, A. M. Urnov, and A. V. Vinogradov, FIAN, Preprint No. 193, Moscow, 1981.
 - [7] M. K. Inal and J. Dubau, *J. Phys. B* **22**, 3329 (1989).
 - [8] J. P. Matte *et al.*, *Phys. Rev. Lett.* **72**, 1208 (1994).
 - [9] O. N. Rosmej, *AIP* **299**, 560 (1994).
 - [10] F. B. Rosmej, *J. Quant. Spectrosc. Radiat. Transf.* **51**, 319 (1994).
 - [11] F. B. Rosmej, *J. Phys. B* **28**, L747 (1995).
 - [12] F. B. Rosmej, *J. Phys. B* **30**, L819 (1997).
 - [13] R. C. Elton *et al.*, *J. Quant. Spectrosc. Radiat. Transf.* **65**, 185 (1999).
 - [14] I. Yu. Skobelev *et al.*, *Zh. Eksp. Teor. Fiz.* **108**, 1263 (1995) [*JETP* **81**, 692 (1995)].
 - [15] L. A. Vainshtein and U. I. Safronova, *ADNDT* **21**, 49 (1978).
 - [16] R. D. Cowan, *Theory of Atomic Structure and Spectra* (University Press, Berkeley, 1981).
 - [17] F. A. Parpia, C. Froese-Fischer, and I. P. Grant, *Comput. Phys. Commun.* **94**, 249 (1996).
 - [18] Y. Yamazaki *et al.*, *J. Phys. Soc. Jpn.* **65**, 1199 (1996).
 - [19] S. Thuriel *et al.*, RIKEN Accel. Prog. Rep. (to be published).
 - [20] M. H. Chen, *ADNDT* **34**, 301 (1986).
 - [21] J. Nilsen, *ADNDT* **38**, 339 (1988).
 - [22] W. Kalkhofen, *Methods in Radiative Transfer* (Cambridge University Press, London, 1984).
 - [23] F. B. Rosmej *et al.*, *JETP Lett.* **65**, 708 (1997).
 - [24] S. Kienle, F. B. Rosmej, and H. Schmidt, *J. Phys. B* **28**, 3675 (1995).